A strategy for automated analysis of passive microseismic data to image seismic anisotropy and fracture characteristics

Andreas Wuestefeld*, Othman Al-Harrasi, James P. Verdon, James Wookey and J. Michael Kendall

University of Bristol, Wills Memorial Building, Queen's Road, Bristol, BS8 1RJ, UK

ABSTRACT

Monitoring of induced seismicity is gaining importance in a broad range of industrial operations from hydrocarbon reservoirs to mining to geothermal fields. Such passive seismic monitoring mainly aims at identifying fractures, which is of special interest for safety and productivity reasons. By analysing shear-wave splitting it is possible to determine the anisotropy of the rock, which may be caused by sedimentary layering and/or aligned fractures, which in turn offers insight into the state of stress in the reservoir. We present a workflow strategy for automatic and effective processing of passive microseismic data sets, which are ever increasing in size. The automation provides an objective quality control of the shear-wave splitting measurements and is based on characteristic differences between the two independent eigenvalue and cross-correlation splitting techniques. These differences are summarized in a quality index for each measurement, allowing identification of an appropriate quality threshold. Measurements above this threshold are considered to be of good quality and are used in further interpretation. We suggest an automated inversion scheme using rock physics theory to test for best correlation of the data with various combinations of fracture density, its strike and the background anisotropy. This fully automatic workflow is then tested on a synthetic and a real microseismic data set.

Key words: Fracture-induced anisotropy, Seismic anisotropy, Shear wave splitting, Reservoir characterisation.

INTRODUCTION

Identifying seismically active zones in rock is of interest for a wide array of applications. Seismic activity is caused by rock failure, which, for example in mines, reduces the stability and thus the safety of excavations. In hydrocarbon reservoirs (grain-scale) cracks and (meso-scale) fracturing can connect the pores of the reservoir rock, creating anisotropic permeability, which influences extraction efficiency. To prevent unwanted leakage, CO_2 storage projects require that cracks do not propagate into the overburden. In geothermal projects, fractures increase not only permeability but also the effective

contact surface, which eases the heat transport from rock to the transfer fluid. In all these cases it is therefore desirable to have a detailed knowledge of crack and fracture geometry, which in turn allows optimization of drilling strategies. Finally, on a more regional scale, these fractures and cracks can form (macro-scale) faults, which increase the hazard in volcanic and seismically active regions.

Naturally, it is desirable to identify and study these active zones *in situ*. Seismic methods offer arguably the best approach. Locating seismic events (i.e., ruptures) offers a rough guide on where these weak zones are. A more complete picture can be achieved by identifying aligned fractures through the observation of seismic anisotropy. Aligned fractures and cracks render the rock anisotropic (Crampin 1984) and the method of shear-wave splitting is perhaps the most direct

*E-mail: andy.wuestefeld@bristol.ac.uk

indicator of anisotropy (Ando, Ishikawa and Wada 1980; Crampin 1984; Silver and Chan 1991; Savage 1999)

Recently, Crampin and Peacock (2008) compiled a review of microseismic shear-wave splitting on a crustal scale. Teanby, Kendall and van der Baan (2004a) used shear-wave splitting to image fracture networks in the North Sea Valhall Field, whilst Al-Harrasi, Wuestefeld and Kendall (2009) and Al-Anboori et al. (2005) were able to characterize the different fracture networks pervading the cap-rock and reservoir of an oilfield in Oman. Holmes, Crampin and Young (2000) used a controlled source shear-wave experiment to image fractures in highly stressed granite and Elkibbi and Rial (2005) used splitting measurements recorded on surface seismometers to characterize the fracturing at The Geysers geothermal field in California.

These studies use manual or semi-automatic processing of the data. With ever increasing station number and recording period, the data sets become too large for effective manual processing. In this paper, we present a strategy on how to automatically determine the anisotropic structure of the rock mass from these passive microseismic data sets. We first point out some considerations regarding preprocessing and then present an automated shear-wave splitting procedure that includes an automated quality assessment. Given sufficient ray coverage, we show that the best measurements can then be used in an automated inversion to determine the anisotropic system. This workflow is tested on a synthetic data set and demonstrated on a real passive seismic data set recorded in a producing oilfield.

CAUSES OF ANISOTROPY

Seismic anisotropy is the directional variation of seismic wave speed and occurs at many different scales, ranging from geologic formations (kilometres) to single-crystal (micrometres). This broad range of spatial scales complicates the imaging efforts of band-limited data. The signal generated by earthquakes has a dominant period that is too long to be sensitive to only the single-crystal anisotropy. Furthermore, the Fresnel zones associated with these dominant periods can sometimes be wider than the characteristic scale of the type of anisotropy. Seismic waves therefore experience an average of the different anisotropies, or 'bulk' anisotropy.

In contrast, seismic isotropy is usually a result of a randomly cracked rock and random crystal or grain orientations. An increasing number of observations support the idea that isotropy is the exception rather than the norm and the rocks generally have to be treated as being anisotropic. In general,

the anisotropy encountered in rocks is triclinic with 21 independent elastic parameters but can be approximated in many situations as having hexagonal symmetry, which can be fully described by five independent elastic parameters.

For simplicity, most geological processes are assumed to result in purely hexagonal anisotropy, which can mainly have four causes:

1 Fractures: a medium with a preferential orientation of meso-scale fractures renders the bulk rock seismically anisotropic (e.g., Hudson 1981; Crampin 1984; Liu et al. 1993; Kendall 1994; Thomsen 1995; Chapman 2003; Kendall et al. 2006). These fractures can be fluid or gas-filled and are generally assumed to be penny shaped (Hudson 1981). The orientation of aligned fractures can be controlled by both the present and past regional stress field. In fractured and cracked rock, the strength of seismic anisotropy is proportional to the crack density (number of cracks of a given radius per unit volume) within the rock body traversed by the seismic wave. The crack density ρ_c varies with the cube of the crack radius, a and is expressed by:

$$\rho_c = Na^3/V, \tag{1}$$

where N is the number of cracks with radius a within a rock volume V (O'Connell and Budiansky 1974; Hudson 1981; Crampin 1984). Assuming a Poisson's ratio of $v = 0.25$ and penny shaped cracks, the crack density is approximately one hundredth of the observed percentage shear-wave anisotropy: $\rho_c = A/100$ (Crampin 1984).

Fluids within the pores, cracks and fractures can have a significant influence on observed anisotropy. This depends on the extend to which pore fluid pressure can equilibrate with the dynamic pressures changes caused by a transient wave and thus rendering the anisotropy frequency dependent (e.g., Zatsepin and Crampin 1997; Guest, van der Kolk and Potters 1998; Pointer, Liu and Hudson 2000; Maultzsch et al. 2003; Chapman 2003; Galvin, Gurevich and Sayers 2007)

2 Grain-scale fabrics: the presence of aligned compliant discontinuities such as (micro-) cracks between individual sedimentary grains can render a rock anisotropic (e.g., Hall et al. 2008). Both the magnitude and alignment of such anisotropy may be modulated by short-term variations of the local stress field, which may be induced by production. (e.g., Vega et al. 2006; Verdon et al. 2008).

3 Mineral alignment: alignment of mineral grains can be induced by a constant deformation direction at relatively high temperatures. This is most likely to occur under conditions found in the lower crust and upper mantle (Hess 1964; Nicolas and Christensen 1987). In sedimentary rocks, the

anisotropy tends to be dominated by clay and mica, which due to their platy nature align horizontally and generate hexagonal anisotropy (e.g., Kaarsberg 1968; Valcke *et al.* 2006; Kendall *et al.* 2007). Other common minerals, such as olivine, quartz or plagioclase, are strictly orthorhombic but have a strong hexagonal component (Mainprice and Silver 1993; Valcke *et al.* 2006), showing a fabric related to deposition or flow direction.

4 Layering: alternating layers of otherwise isotropic material renders the rock anisotropic at a wavelength greater than the characteristic thickness of the layers (Backus 1962). This is of particular interest in hydrocarbon reservoirs as they are mostly located in sedimentary environments. The strength of anisotropy is proportional to the velocity difference of the layers and their relative thickness.

In geology, rarely only one of these four causes is responsible for the observed anisotropy. A more realistic assumption is a superposition of these mechanisms, which will result in orthorhombic or higher symmetry systems. An orthorhombic symmetry has three different, mutually perpendicular symmetry axes of seismic velocities. Hexagonal symmetry in contrast has a plane of isotropic velocities. It has become standard in literature to classify hexagonal anisotropy by the orientation of its axis of isotropy, that is, TTI, HTI and VTI for respectively tilted, horizontal and vertical transverse isotropy (Fig. 1). Shear waves travelling parallel to this axis of symmetry are not split. VTI media may also be referred to as having azimuthal isotropy, polar isotropy or radial anisotropy.

When sounding an anisotropic rock at various angles, the variation in fast shear-wave polarizations and delay times reveals the anisotropic symmetry axes and strength of anisotropy (Fig. 2). This in turn allows the deduction of rock physics parameters such as the fracture and crack orientation and densities. Verdon, Kendall and Wuestefeld (2009) showed that certain combinations of anisotropy systems and illumination directions are better suited to invert for rock physics parameters than others.

SHEAR-WAVE SPLITTING

It is well described in literature that a shear wave passing through an anisotropic medium is split into two mutually orthogonal waves (e.g., Crampin 1984; Savage 1999). The two waves are polarized along the anisotropic symmetry axes and are separated by a delay time proportional to the strength of anisotropy. This is described by the two splitting parameters Φ and dt. The strength of anisotropy is generally reported
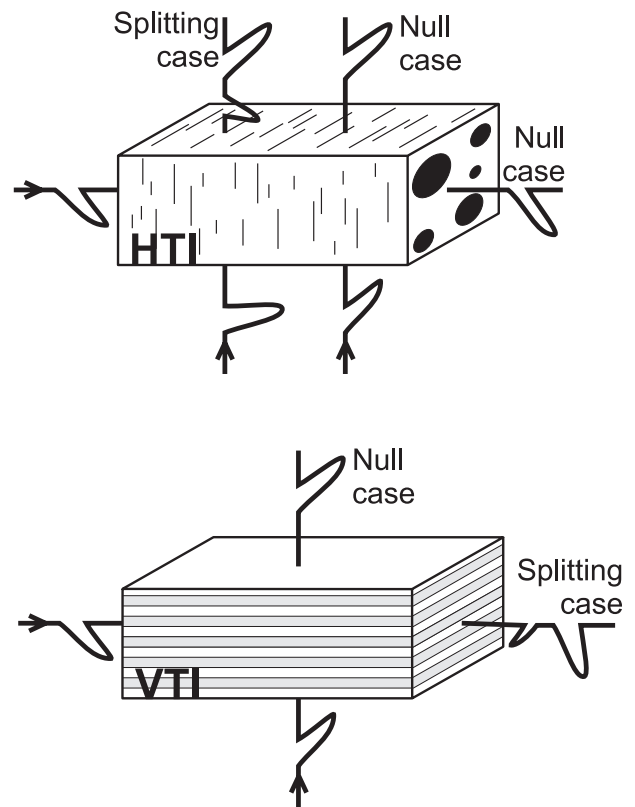

Figure 1 Shear-wave splitting in two common hexagonal anisotropic symmetry systems, HTI and VTI. Shear-wave splitting occurs for characteristic ray directions. Specific combination of symmetry axis and initial polarization will cause null splitting results.

in per cent (shear-wave) velocity variation by the common approximation:

$$A = V_{Smean}dt100/r, \tag{2}$$

where r is the source-receiver-distance, V_{Smean} is the mean S-wave velocity and dt is the delay in arrival time between waves polarized along the fast and slow symmetry axes.

In the literature a number of nomenclatures for Φ, the 'polarization orientation of the fast shear-wave' have been proposed, all meaning more or less the same but are sometimes an oversimplification. Strictly, the use of 'fast direction' is wrong in that a direction is a vector with 360° periodicity. Although 'fast orientation' or 'fast axis' accounts correctly for the 180° periodicity in data, this nomenclature remains ambiguous on whether P- or S-velocities are analysed. Furthermore, no distinction is possible between the fast orientation in the ray frame and geographical coordinates, which is strictly only identical for vertical wave propagation. We therefore suggest using 'fast S-wave polarization' (Φ) if in the ray frame and
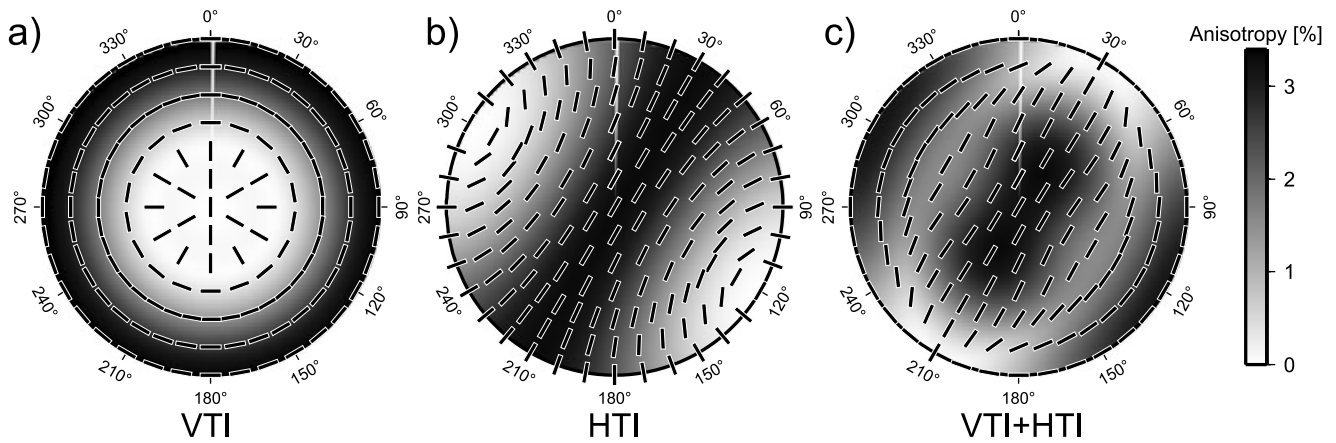
Figure 2 Synthetic upper hemisphere plots for respectively HTI, VTI anisotropy and a combination of both. Shading indicates relative strength of shear-wave velocity anisotropy (in per cent). Black bars represent the fast S-wave polarization.
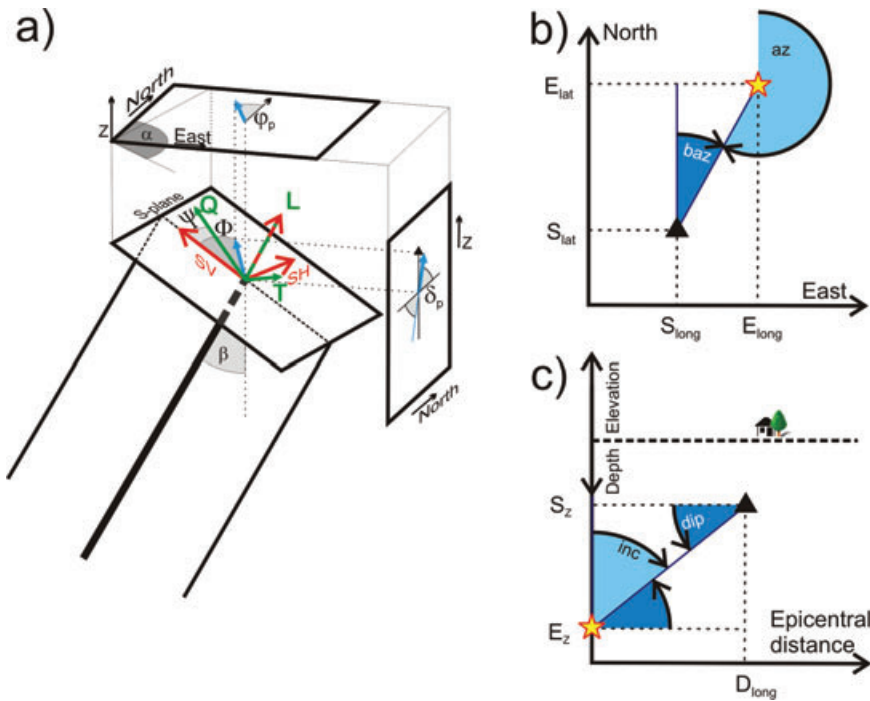

Figure 3 Coordinate systems and associated angles used in shear-wave splitting. a) Wave coordinates and orientation of fast polarization in the ray plane and projection to geographical coordinates (modified after Vecsey *et al.* 2007). We assume the right-handed coordinate system East-North-Up, L-SH-SV and L-T-Q. See Table 1 for nomenclature. Schematic map view (b) and cross-section (c) define the geometric angles.

'strike of fast S-wave polarization' (φ_p) in geographical coordinates, as illustrated in Fig. 3. Note that these orientations do not always coincide with the actual fast symmetry axis of the medium (Fig. 2). In Table 1 we summarize the symbols and conventions used in this paper. The main angles involved in these definitions can then easily be calculated as

$$baz = \alpha' = atan_2(E_{long} - S_{long}, E_{lat} - S_{lat})$$

$$az = \alpha = 180 + \alpha'$$

$$D = \sqrt{(E_{long} - S_{long})^2 + (E_{lat} - S_{lat})^2}$$

$$inc = \beta = \arctan\left(\frac{D}{E_{Depth} - S_{Depth}}\right)$$

$$= \arctan\left(\frac{D}{S_{Elevation} - E_{Elevation}}\right)$$

$$dip = \theta = 90 - \beta, \tag{3}$$

Table 1 List of symbols used in this paper

Symbol	Description	Unit
α	Azimuth	°
α'	Backazimuth	°
β	Inclination	°
δ	Thomsen's parameter	
ε	Thomsen's parameter	
γ	Thomsen's parameter	
λ	Eigenvalues	
ν	Poisson's Ratio	
Ψ	Separation between backazimuth and initial polarisation of S-Wave	°
ρ_c	Crack density	
δ_c	Crack Dip	°
φ_c	Crack Strike	°
δ_p	Dip of Fast polarisation plane	°
φ_p	Strike of Fast polarisation plane	°
Φ	Fast polarisation in SV-SH plane	°
dt	Delay time between fast- and slow wave	sec
Ω	Normalised separation of Cross-correlation and Eigenvalue fast axis orientation	
Δ	Ratio of Cross-correlation and Eigenvalue delay times	
Γ	Quality threshold	
Q	Quality of the measurement	
A	Percentage Anisotropy	%
D	Epicentral distance	m
a	Aspect ratio of a crack	
r	Straight line source-receiver distance	m
HTI	Horizontally Transverse Isotropy: Hexagonal anisotropy with horizontal axis of symmetry	
VTI	Vertically Transverse Isotropy: Hexagonal anisotropy with vertical axis of symmetry	
E-N-Z	Seismogram components in geographical (East-North-Vertical) coordinates	
L-T-Q	Seismogram components in natural coordinates, (Ray-parallel, Transverse in S-plane and parallel to S-wave polarisation)	
L-SH-SV	Seismogram components in ray coordinates (Ray-parallel, horizontal and vertical transverse components in S-plane). SV is in the sagittal plane and not necessarily strictly vertical.	

where *az* and *baz* refer to azimuth and backazimuth, *inc* is the inclination of the wave from vertical and *dip* is the dip of the wave from horizontal. *E* and *S* describe event and station coordinates, respectively and *D* is the (Cartesian) hypocentral distance. Note that the inclination β is always defined as positive from vertical up towards the azimuth α, or due to symmetry positive from vertical down towards the backazimuth α'. The two-argument function atan$_2$ calculates the arc-tangent of the two parameters similar to calculating the arc-tangent except that the signs of both arguments are used to determine the quadrant. This results in 360° periodicity for the atan$_2$ function instead of 180° periodicity for the arc-tangent.

Two complementary types of techniques exist for estimating the splitting parameters Φ and dt. The first type (multi-event technique) simultaneously analyses a set of records coming from differing azimuths. Vinnik et al. (1989) proposed to stack the transverse components with weights depending on azimuths. However, this method lacks a means of constraining measurement errors. Chevrot (2000) projected the amplitudes of the transverse components (Fig. 3) to the amplitudes of the time derivatives of radial components to obtain the so-called splitting vector. The phase and amplitude of the best fitting curve gives the fast S-wave polarization and delay time, respectively. These multi-event techniques are generally applied in some teleseismic studies (Vinnik 1989; Dricker *et al.* 1999; Long and van der Hilst 2005).

More versatile is the second type of technique, which determines the anisotropy parameters on a per-raypath basis (Ando *et al.* 1980; Fukao 1984; Silver and Chan 1991; Menke and Levin 2003). A grid search is performed for the splitting parameters that best remove the effect of splitting. Different measures for 'best removal' exist.

The first is the cross-correlation technique (XC hereafter), which rotates the seismograms in test coordinate systems and searches for the orientation where the cross-correlation coefficient is maximum and thus returning the splitting parameter estimates Φ_{XC} and dt_{XC} (e.g., Ando *et al.* 1980). This technique can be visualized as maximizing the similarity in the non-normalized pulse shapes of the two corrected seismogram components.

The second technique searches for the most singular covariance matrix of rotated and time-shifted seismograms based on its eigenvalues λ_1 and λ_2 (EV hereafter; Fukao 1984). Silver and Chan (1991) emphasized the similarity of a variety of such measures such as maximizing λ_1 or λ_1/λ_2 and minimizing λ_2 or λ_2/λ_1. We found that minimizing λ_2/λ_1 gives the most robust results for the splitting parameter estimates Φ_{EV} and dt_{EV}.

Wuestefeld and Bokelmann (2007) identified characteristic differences between the two techniques (XC and EV) close to 'null' directions. Such null measurements occur either if the wave propagates through an isotropic medium or if the initial S-wave polarization direction coincides with the projection of an anisotropic symmetry axis. In these cases the incoming shear-wave is not split (Fig. 1). For initial polarizations deviating from the null directions the results of both methods should be similar. The difference between the two techniques depends on the signal-to-noise ratio (S/N) and the deviation from a null direction.

The confidence in the splitting result can be increased by stacking multiple error surfaces. Stacking can be done with the normalized error surfaces (Wolfe and Silver 1998), error surfaces weighted by signal-to-noise ratio (Restivo and Helffrich 1999) or directly adding individual error surfaces (Wuestefeld 2007), since the variation of peak-to-peak amplitude of the error surface topography between individual measurements acts as a form of weighting. Teanby *et al.* (2004a) stacked the results form neighbouring stations in a vertical borehole array setup.

AUTOMATION APPROACHES

There are various aspects and pitfalls associated with shear-wave splitting analysis, such as cycle skipping, correlated noise and window selection (Vecsey *et al.* 2007). Thus far, most splitting measurement workflows include manual steps, such as visual quality control of wave forms and/or diagnostic plots (Teanby *et al.* 2004b; Gao, Hao and Crampin 2006; Evans, Kendall and Willemann 2006; Wuestefeld *et al.* 2008). With ever increasing sizes of data sets, this is becoming impractical.

Furthermore, the increase in data volume provides a more detailed sounding of the region of interest and thus, instead of simple statistical analysis of splitting parameters, allows for a systematic inversion for plausible anisotropy systems and hence a variety of rock physics parameters (Verdon *et al.* 2009).

Here, we present an automated approach for evaluation of shear-wave splitting measurements that is based on using both the EV and XC method to estimate the splitting parameters. The XC method systematically fails close to null directions, which is a result of the absence of S-energy on the transverse component close to nulls. Correlation can only be found if the test-rotations of the grid search 'copy' energy from the initial polarization component to the transverse component. Thus the correlation is maximum for a test rotation of 45° and obviously results in zero timelag between the two components (see Wuestefeld and Bokelmann (2007) for a detailed discussion). We here modify the automated null detection technique proposed by Wuestefeld and Bokelmann (2007) to give a numerical value for quality. First, we calculate the delay time ratio $\Delta = dt_{XC}/dt_{EV}$ and the normalized differences in fast S-wave polarization estimate $\Omega = (\Phi_{EV} - \Phi_{XC})/45°$. Thus ideal 'good' measurements are characterized by identical delay times and identical fast polarization estimates (i.e., $\Delta = 1$, $\Omega = 0$) in both methods. In contrast, for ideal 'null' measurements the XC method shows no delay time ($dt_{XC} = 0$) whilst the fast polarizations differ by 45° (i.e., $\Delta = 0$, $\Omega = 1$). The quality, Q_W, of an individual measurement is determined from the distance, d_{null} and d_{good}, to these extreme points (Fig. 4):

$$
\begin{aligned}
d_{null} &= \sqrt{\Delta^2 + (\Omega - 1)^2}\sqrt{2} \\
d_{good} &= \sqrt{(\Delta - 1)^2 + \Omega^2}\sqrt{2} \\
Q &= \begin{cases} -(1 - d_{null}) & \text{for } d_{null} < d_{good} \\ (1 - d_{good}) & \text{for } d_{null} \geq d_{good}. \end{cases}
\end{aligned}
\tag{4}
$$

Distances greater than one are set fixed to 1, so they result in a quality of $Q_W = 0$. Thus, the quality ranges from +1 (good) to 0 (poor) to −1 (good null). Figure 4 illustrates this calculation for the example of a synthetic data set that is later discussed in detail. The positions of the individual measurements in the quality plane are shown as black dots.

This automated quality control is incorporated into the multi-window cluster analysis described by Teanby *et al.* (2004b). They point out that the splitting parameters can vary with the choice of the S-window and propose an automatic analysis of the splitting parameters for many (usually between
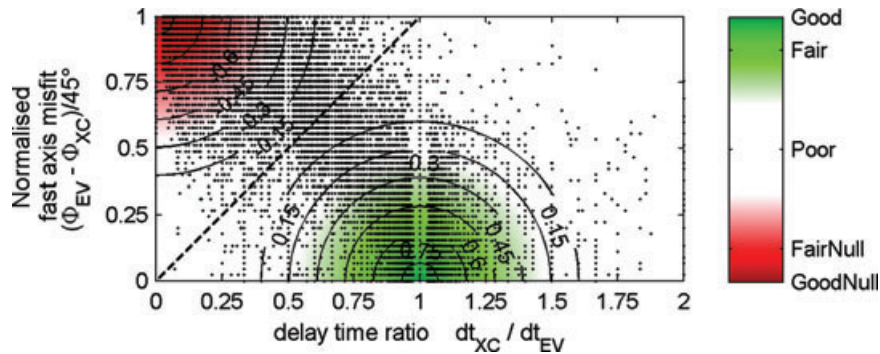
Figure 4 The automatic quality detection of a measurement is based on characteristic differences between the XC and EV splitting technique. Depending on the distance from any of the two extreme points we are thus able to assign a quality. Note that most measurements align along the extreme points. Outliers are due to poor signal-to-noise ratio or uncertainties in ray coordinate rotations as a consequence of poor P-particle motion.

100–250) S-wave windows. In order to determine the 'best' splitting measurement, one possibility is to use stacking procedures (Wolfe and Silver 1998; Restivo and Helffrich 1999; Teanby *et al.* 2004a; Wuestefeld 2007). Null measurements ($Q < 0$) should probably be excluded to prevent contamination, since experience shows that error surfaces of nulls have generally a steeper topography (greater peak-to-peak amplitude) than non-nulls. The final splitting parameter will be determined from the minimum in the stacked error surface, which may however show a complex topography. Alternatively, the best measurement can be simply defined as that with the highest Q_{Win} but such a definition is problematic when detailed information about null measurements is required.

We thus suggest here to use the cluster analysis of Teanby *et al.* (2004b) and determine the 'best' splitting measurement from clusters of similar splitting parameters and choosing that with the lowest variance. Then, to each of the N test splitting windows a quality value Q_{Win} between -1 and $+1$ is assigned. The quality Q_{best} of the measurement closest to the cluster midpoint is determined separately. In order to account for events with a few problematic S-wave windows, we define the overall quality of the event as a weighted average of Q_{best} and the mean of the individual measurements:

$$Q_{event} = \omega_1 \frac{\sum Q_{Win}}{N} + \omega_2 Q_{best}. \qquad (5)$$

The factors $\omega_{1,2}$ determine the weight of the average and best quality, respectively. We suggest using values of $\omega_1 = 1/3$ and $\omega_2 = 2/3$.

NULLS

Null measurements represent cases where the shear wave is not split. Although generally neglected, null measurements never-

theless bear important information about the anisotropy of the rock (Wuestefeld and Bokelmann 2007). Nulls occur if a) the wave travels through an isotropic medium, b) the initial polarization of the shear wave coincides with an anisotropic symmetry axis or if c) the wave travels along an (isotropic) symmetry axis of the medium (see Fig. 1). Furthermore, the effective anisotropy encountered by a seismic wave is a function of ray direction (Fig. 2). Ray directions with lower anisotropy should therefore produce characteristically more nulls at a similar signal-to-noise ratio since the resolution limit of the splitting method is reached. Nulls thus have significant potential to further constrain the anisotropy of the rocks in future developments of automated splitting.

Note that with decreasing signal-to-noise ratio the split shear wave increasingly resembles a null measurement. This is because no distinctive pulse is split or the amplitude of the secondary S-wave is masked by the noise level. Thus far, we must reject these 'noise nulls'. We can achieve this by comparing the initial polarization with the observed fast direction and the signal-to-noise ratio before and after correction. 'Real nulls' (parallel symmetry axis and initial polarization) generally also show large EV and very small XC delay times, resulting in quality values of close to -1, whereas 'noise nulls' have quality values closer to -0.5. Note, that the observation of nulls from all directions and initial polarizations indicate an isotropic medium.

STATION GEOMETRY AND EXPERIMENT SETUP

The best experiment setup is obviously a permanent, regularly spaced 3D array of high-sampling rate, broadband sensors located around and within the expected seismogenic zone.
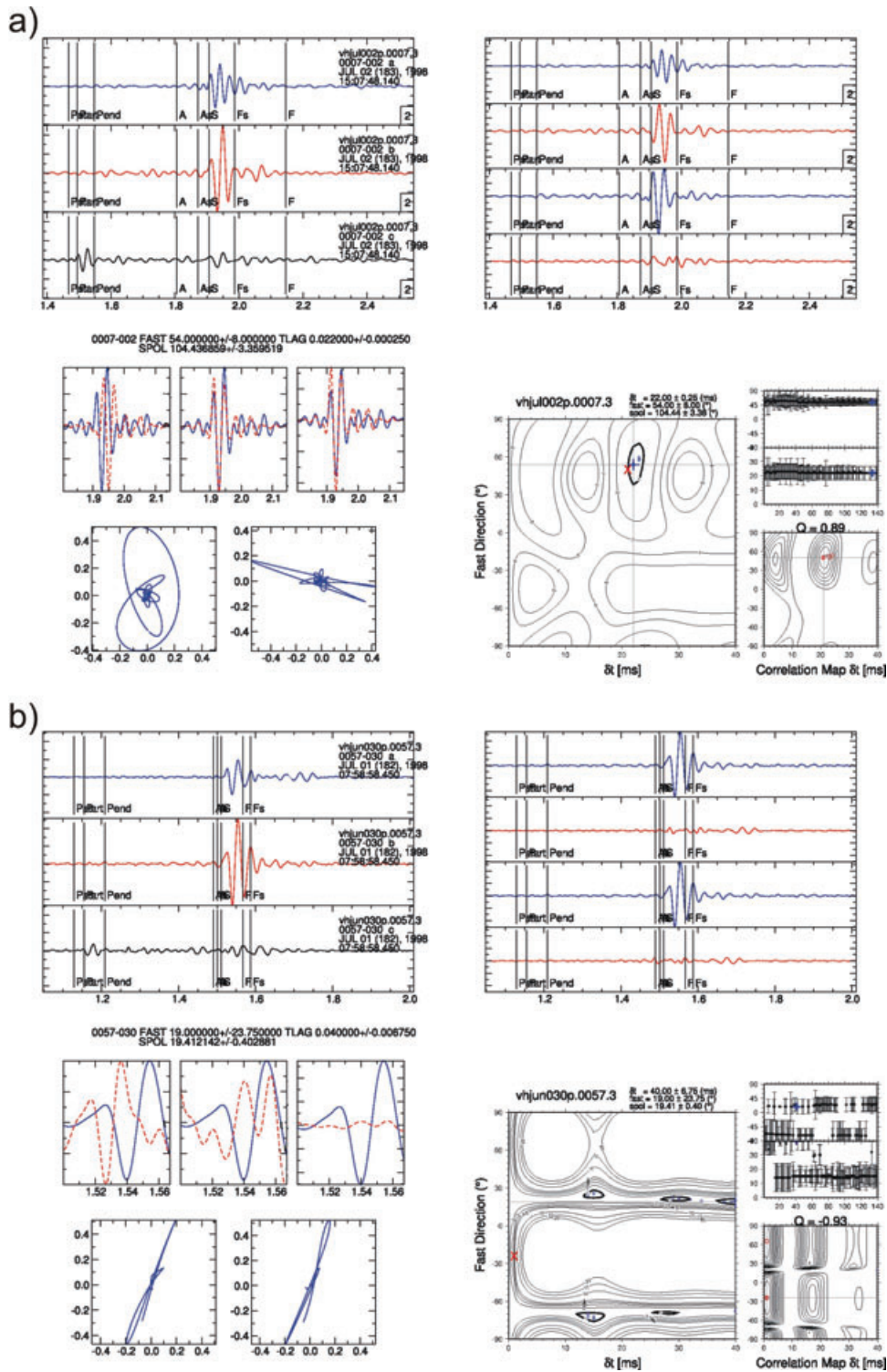
Figure 5 Diagnostic plot for the example of a good (a) and null (b) shear-wave splitting measurement. The top left panel shows SH (blue), SV (red) and ray (black) seismogram components and P and S windows. The top right panel shows radial (blue) and transverse (red) component before (top two traces) and after (bottom) splitting correction. The lower left panel shows the particle motion in SH–SV coordinates before (left) and after (right) correction. Finally, the lower right panel shows the error surfaces of the eigenvalue (left) and cross-correlation (lower right) methods. These represent the error surfaces of the respective best measurements. The location of the minimum is indicated by thin black lines

Following equation (2), a minimum percentage anisotropy of $A = 2\%$ corresponds to a delay time of $dt \approx 2 * r/100/V_{Smean}$. Typical S-wave velocities are in the order of 2000 m/s, resulting in expected delay times of 10 μs per metre raypath length. For typical source-receiver distances of 100 m that requires at least a sampling rate of 1000 Hz. A detailed discussion may be found in Gibowicz and Kijko (1994). This ideal 3D array setup is probably only possible in mining environments where galleries allow easy access.

Eisner *et al.* (2009) presented a study on the accuracy of event locations for various source-receiver geometries at a single borehole situation. As shown below, the interpretation of shear-wave splitting measurements requires reasonable directional coverage. If prior knowledge of the anisotropy is available the experiment design can be adopted accordingly. For example, near-vertical fractures are best mapped with near-vertically travelling rays. Verdon *et al.* (2009) pointed out that minimal ray coverage from strategically planed directions can be sufficient for a successful inversion.

SUGGESTED WORKFLOW FOR FULLY AUTOMATED SHEAR-WAVE SPLITTING

We presume that the P- and S-wave arrivals have previously been picked and only traces with both picks available can be used. The P-pick is used for seismogram rotations (as discussed below) and obviously the S-pick serves as the basis for the shear-wave window to be analysed for splitting. Also, we assume that each of the traces to be analysed has a known event location. Having both event location and P- and S-picks available in all traces can also be regarded as an inherent 0th-order quality control since only traces of reasonable quality allows detection of both phases, especially if an auto-picker and auto-locator is used. Furthermore, consistently rejecting lowest quality traces from the data base significantly reduces the computational costs.

The following steps are required to develop a consistent input data set and the necessary parameters for an automated splitting analysis. As a first step we recommend filtering out any electrical noise from the raw, unrotated seismograms (see

Appendix). The characteristic relationship between source-receiver distance and S-wave amplitude decay for the reservoir in question should then be determined (Al-Harrasi *et al.* 2009). This serves as a basis for the minimum length of the splitting window. The maximum delay time in the grid-search, dt_{max}, should be chosen based on the dominant frequency of the S-waves. As a rule-of-thumb, this dt_{max} is approximately half the average dominant period of the S-wave but can vary largely. Finally, the window length for cluster analysis (Teanby *et al.* 2004b) should be chosen. Note that the shortest possible window must be longer than dt_{max} to avoid the wavelet being shifted out of the analysis window. Obviously, overlapping the P- and S-wave window and contamination with reflected or refracted waves has to be avoided.

After these preprocessing and configuration steps the automated splitting is performed in four steps:

1 Rotation from sensor to geographical reference frame (X-Y-Z to E-N-Z) by using check shots. If these are not available compare P-particle motion with straight line polarizations.

2 Rotation from geographical to ray reference frame (E-N-Z to L-SH-SV, see Fig. 3) by maximizing particle motion in the P-window on one component (e.g., Vidale 1986; Jurkevics 1988). Note that this approach shows a 180° ambiguity of the resulting polarization direction. This ambiguity can be eliminated by identifying the correct quadrant using the event locations or by incorporating the dip information of particle motion in the inversion (Jones *et al.* in press).

3 Shear-wave splitting analysis using the cluster analysis for multiple (100–250) test windows as described in Teanby *et al.* (2004b). For very short source-receiver distances make sure that the S-window does not include P-energy. The splitting parameters (Φ, dt) are determined by two different techniques, the cross-correlation and eigenvalue method. Simultaneously, the initial polarization of the corrected shear wave is determined from the corrected traces.

4 Quality determination by comparing the results of the two techniques and the selection of the 'good' measurements for further interpretation.

This is repeated for each event of every station, to obtain a complete data set of shear-wave splitting parameters. Figure 5

Figure 5 (continued) and the individual results of the cluster windows are shown as circles. Additionally, the best result of the two methods are shown in both plots as blue '+' and red 'x' for eigenvalue and cross-correlation respectively. The upper right diagrams represent the fast axis (top) and delay time variations for each window and include the corresponding error bars. Note the reduction of energy on the transverse component and the linear particle motion. Furthermore, the two correction methods (XC and EV) give the same result in a) and different in b). Small error bars indicate a clear and stable measurement. The null measurement in (b) has linear particle motion from the onset. Note the small delay time estimates for the XC method and 45° difference in the fast orientation estimate. Cycle skipping causes repetitive patterns in the error surfaces of both methods. See text for discussion.

shows a diagnostic figure illustrating all steps of the splitting process.

The proposed method of testing various windows around the S-pick renders the results independent of picking accuracy. However, the resolution of delay time and thus anisotropy is limited by the sampling rate of the seismogram. Most uncertainty in the determination of anisotropy is introduced through the accuracy of event location and, to a smaller extent, the velocity model (equation (1)). Manual quality control suggests that generally only around 10% of a given data set produces good measurements, although that may vary with wave form quality and picking accuracy. For further analysis, we thus consider only measurements that have a quality value Q above a certain threshold, which we denote Γ. Obviously, this threshold can be varied if the data set is exceptionally large or small. The overall signal-to-noise ratio of the data set should be taken into account. We suggest using a threshold of $0.75 \leq \Gamma \leq 0.9$.

VERIFICATION USING A SYNTHETIC MODEL

We first test the automated workflow for processing and interpreting split shear waves on three synthetic data sets. In accordance with Fig. 2, we simulate seismic waves passing through a HTI and/or VTI medium within a background matrix with $v_P = 3.009$ km/s, $v_S = 1.654$ km/s and $\rho = 2340$ kg/m^3. Thomson's anisotropic parameters for the VTI are $\varepsilon = 0.013$, $\gamma = 0.033$ and $\delta = -0.001$. These parameters

of the background matrix correspond to sandstone shale as given in Thomsen (1986). The HTI medium simulates vertical cracks striking at 30°N with a crack density of $\rho_c = 0.031$.

The waves arrive at the station from all ranges of backazimuths and inclinations in steps of 10° (cf. Fig. 2). For each direction we simulated 20 seismograms of initial polarizations between $-45°$ and $+45°$ to mimic variation of source mechanisms. We repeated this for 4 different signal-to-noise ratios (S/N) between 2.5–20. Thus the synthetic data set consists in 28 800 3-component seismograms. Figure 6 shows the upper hemisphere plots of the mean quality for the different models. For each direction the mean quality of the 20 rays with different initial polarization is calculated. As a threshold we choose $\Gamma \geq 0.75$ for good and $\Gamma \leq -0.75$ for null measurements.

The reliability of the automation can be assessed by comparing the automatically assigned quality Q with the separation Ψ between observed initial polarization and estimated fast S-wave polarization. For a separation of $\Psi = 45°$, we expect the effect of splitting to be strongest and thus the highest quality of measurements, whereas for $\Psi = 0°$ and $\Psi = 90°$ we expect nulls. Figure 7 shows a map of the distribution of results in the Ψ-Q plane. The automated quality control robustly assigns the correct quality. It shows that a separation from the null direction of approximately $\Psi > 20°$ is required for splitting to be reliably detected. This now allows the selection of a suitable threshold for a reliable measurement. These 'good' measurements can then be used for interpretation and we suggest below an automated interpretation procedure that inverts for best fitting rock physics parameters.
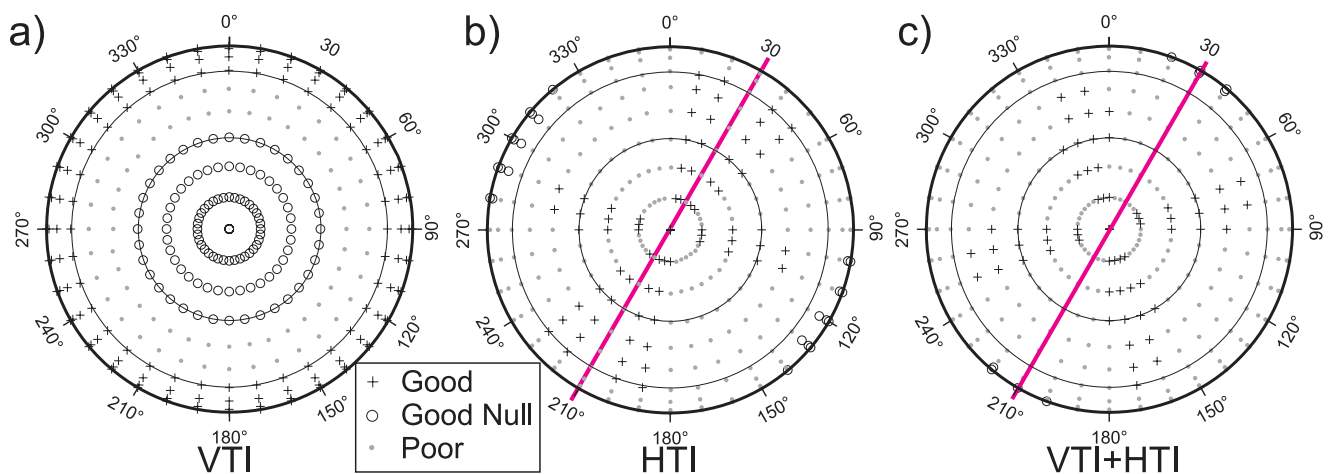

Figure 6 Distribution of mean splitting measurement quality in upper hemisphere for synthetic VTI, HTI and VTI+HTI media. Crosses indicate 'good' mean quality ($\Gamma > 0.75$) and circles 'good nulls' ($\Gamma < -0.75$). The remaining unconstrained measurements are represented as dots. The bar in b) and c) indicates the strike of the HTI plane of isotropy.
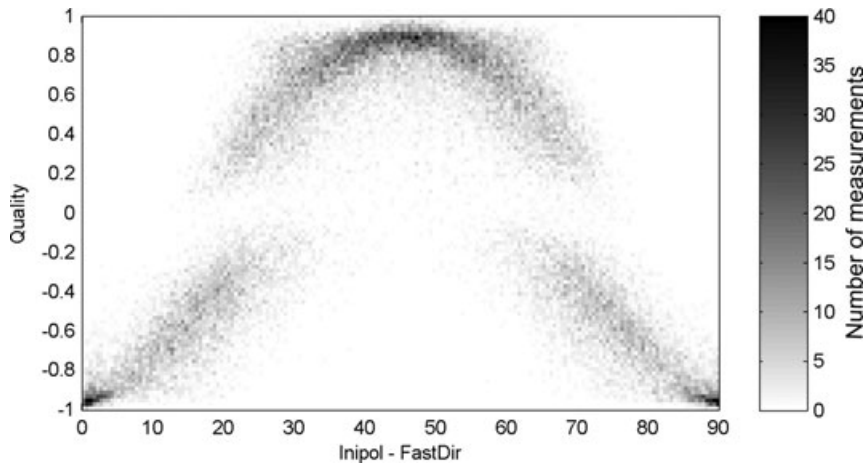
Figure 7 Result density map (or 2D histogram) of a synthetic data set of 28 800 measurements of varying source polarization and signal-to-noise ratios through an HTI medium. The colour represents the number of measurements within a cell of a certain combination of quality value and initial polarization. Note that good measurements require a separation between source polarizations and fast orientation of 30–60° and nulls generally have a separation of 20° from source polarization. The signal-to-noise ratio strongly affects these limits.

AUTOMATED INVERSION

The measurement of Φ and A as outlined above can never be the conclusion of a shear-wave monitoring experiment. The shear-wave splitting observations must be interpreted in terms of subsurface structure. When dealing with large quantities of data that are generated by automated splitting analysis, interpretation presents its own difficulties. Traditionally, when interpreting shear-wave splitting measurements it is assumed that Φ directly relates to the strike φ_c of a set of aligned cracks, with increasing A representing an increase in crack density ρ_c. However, Fig. 2 shows that the interaction between various fabrics and shear waves travelling at arbitrary angles in the subsurface is complicated, often unintuitive and always non-linear. Modelling the anisotropic structure using rock physics theory helps with reliably interpreting the observations. Rather than relying on 'chi-by-eye' in comparing models with observations, automated inversions (Sileny and Plomerova 1996; Verdon *et al.* 2009) allow systematic exploration of the whole parameter space. This becomes particularly crucial when dealing with large data sets, where at first glance the results can often appear as a cloud, with patterns and structure not immediately obvious. How well the subsurface structure is imaged is highly dependent on the range of arrival angles available in the data set (Verdon *et al.* 2009). For instance, from Figs 1, 3 and 6 it is clear that near-vertical waves will do a good job of imaging vertical fractures but will not be able to image VTI fabrics. In this section we outline a procedure for interpreting automated shear-wave splitting observations.

The type of rock physics model to be used in inversion should be dependent on the geological setting in question. For instance, in hydrocarbon reservoirs, the most important causes of anisotropy are aligned VTI sedimentary fabrics and aligned vertical fractures. Hence, the free parameters in the inversion are the strength of the VTI anisotropy, as given by Thomsen's (1986) γ and δ parameters, the strike of the fractures, φ_c and the fracture density ρ_c. Alternatively, in some settings it may be more appropriate to invert for two sets of vertical fractures each with strike $\varphi_{c(1,2)}$ and density $\rho_{c(1,2)}$. In hard rock and geothermal settings nearer to the surface, fractures are more likely to be dipping and VTI is less common, so the free parameters become the fracture density, strike and dip. There is no conceptual reason why the complexity of the inversion could not be increased with the inclusion of further fabrics. However, the inclusion of extra degrees of freedom beyond those mentioned above often only leads to trade-offs between parameters, rather than any significant reduction of misfit between the observed and modelled splitting measurements.

Such inversion completes the automated splitting workflow (Fig. 8). We follow the method outlined in Verdon *et al.* (2009) by performing a grid search over the free parameters chosen (φ_c, ρ_c, γ and δ in this case) and for each case we compute the full 81 components of the elastic stiffness tensor. Note that a grid search may not be the most computationally effective approach but offers some protection against local minima. We fix Thomson's ε to $\gamma/2$, as ε does not affect S-waves. For each elastic model the Christoffel
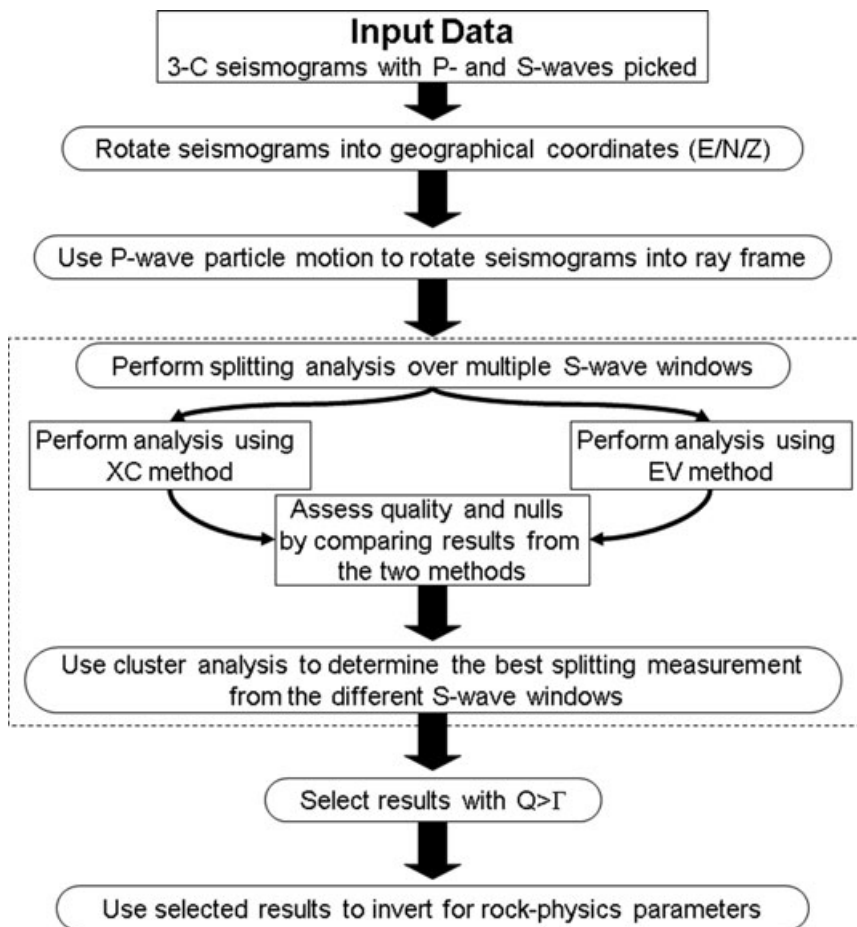
Figure 8 Workflow of fully automated shear-wave splitting with quality control.

equation is solved to compute the splitting parameters (Φ and A) for each arrival azimuth and inclination observed in the data set. The misfit between modelled and observed Φ and A is computed for each observation and summed to give the overall rms misfit. Figure 9 shows the result of such an inversion for an orthorhombic, VTI plus HTI, medium as shown in Fig. 2. Directional coverage with good splitting measurements is excellent, as every possible direction is covered by several initial polarizations of the S-wave. The crack strike is well recovered, crack density and γ are slightly underestimated.

APPLICATION TO REAL DATA: VALHALL OILFIELD

In this section we compare the results of the automation to a previous manual analysis of the Valhall Oilfield in the North Sea. Valhall is an overpressured, undersaturated Upper Cretaceous chalk reservoir. The microseismicity mainly oc-

curs in the overlying siltstone cap-rock and is a consequence of production-induced subsidence. Six seismometers were installed in a vertical monitoring well outside and above the seismogenic zone. 324 events could be located during the 56 days recording period (Dyer *et al.* 1999), yielding 1908 usable records.

The manual approach of Teanby *et al.* (2004a) uses stacking of the error surfaces from individual events of the top three sensors to improve result quality, resulting in 144 reliable measurements. Further restricting the maximum accepted error, yields 117 and 110 reliable measurements for Φ and dt respectively. Using this method, the authors inferred a single set of vertical cracks oriented N65°E and maximum delay times of 20 ms, or 2.5% anisotropy.

The automation allows easy variation of input parameters and we tested the data set with different band-pass filters (Maultzsch *et al.* 2003; Chapman 2003) with a lower frequency of always 5 Hz and upper filter frequencies of 20 Hz, 30 Hz, 35 Hz, 40 Hz, 45 Hz, 50 Hz and 100 Hz. In order
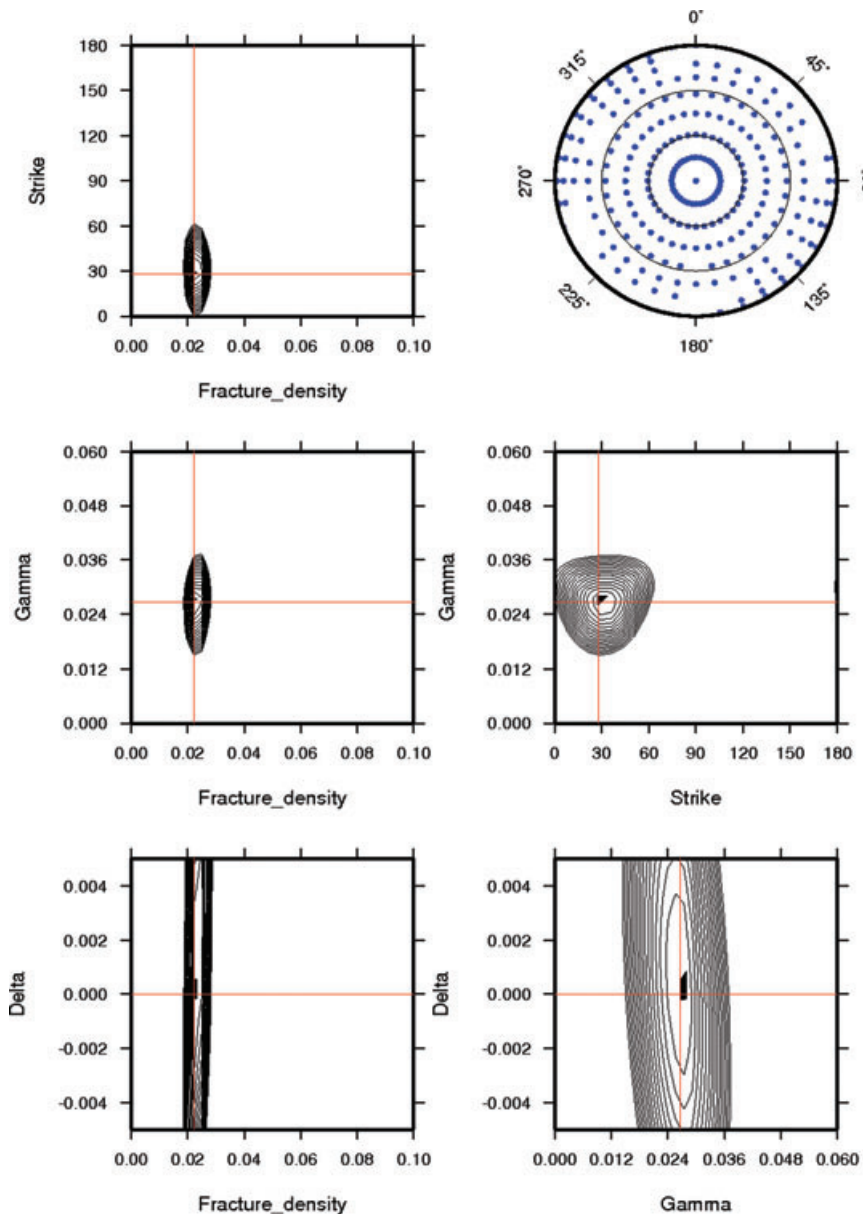
Figure 9 Inversion results for the VTI+HTI model. The upper right plot gives an upper hemisphere projection of the arrivals used in splitting analysis. In the other panels we plot the RMS misfit between observation and model as a function of fracture density, fracture strike and Thomsen's γ and δ parameters. The 90% confidence interval is marked in bold and the best fit model is indicated by red lines.

to mimic the results by Teanby *et al.* (2004b) we restricted the maximum delay time to 20 ms and 40 ms, respectively (see Table 2). Figure 10 shows the histogram of delay times for the XC and EV methods for the different parameter sets. Note the large amount of very small XC delay times and maximum possible EV delay times for all parameters, representing null measurements. These peaks are more pronounced for the 40 ms tests. In combination with the peak at maximum XC delay times for both 20 ms tests, this indicates that limiting

the maximum delay to 20 ms will miss useful results and underestimate the percentage anisotropy and eventually fracture density and/or VTI strength.

One important problem, especially when working with band-limited data, is cycle skipping (Teanby *et al.* 2004b; Vecsey *et al.* 2007). This effect can be observed in the Valhall data set particularly well for the 50 Hz, 40 ms test (Fig. 10b,f) by a minimum of estimated EV-delay times at approximately 16 ms. The panels on the right-hand side of

Table 2 Results of the automated splitting inversion of the Valhall data set using different filters and maximum delay times

	Number of good	φ_c	ρ_c	γ	δ
20 Hz 40 ms	92	75°	0.075	0.020	0.02
30 Hz 40 ms	231	110°	0.105	0.145	0.06
35 Hz 40 ms	260	115°	0.100	0.085	0.05
40 Hz 40 ms	261	115°	0.100	0.135	0.05
45 Hz 40 ms	213	135°	0.095	0.085	0.04
50 Hz 40 ms	173	165°	0.090	0.065	0.04
100 Hz 40 ms	140	170°	0.085	0.070	0.04
30 Hz 20 ms	60	60°	0.045	0.020	0.15
50 Hz 20 ms	141	170°	0.040	0.055	0.02
100 Hz 20 ms	125	140°	0.040	0.050	0.02

Fig. 10(e–h) show the distribution of the dominant frequencies of the signal within the best S-window. This shows a Gaussian distribution of dominant frequencies centred around 32 Hz. It is thus obvious that the minimum in EV-delay times is caused by cycle skipping (Fig. 5) but it is impossible to judge the 'correct' delay time. However, the spike at 20 ms in XC- and EV delay times for the tests limited to a 20 ms delay supports the assumption that such limitation underestimates the true anisotropy and misses a non-negligible amount of large delay time measurements. Furthermore, two estimates of a delay time from two independent splitting methods add confidence to the result. Cycle skipping affects the delay time estimate and hence the strength of anisotropy, while the fast orientation estimate can be 90° wrong. In our inversion technique cycle skipping may only affect the resulting fracture density and VTI strength but not the inferred crack strike (Fig. 11).
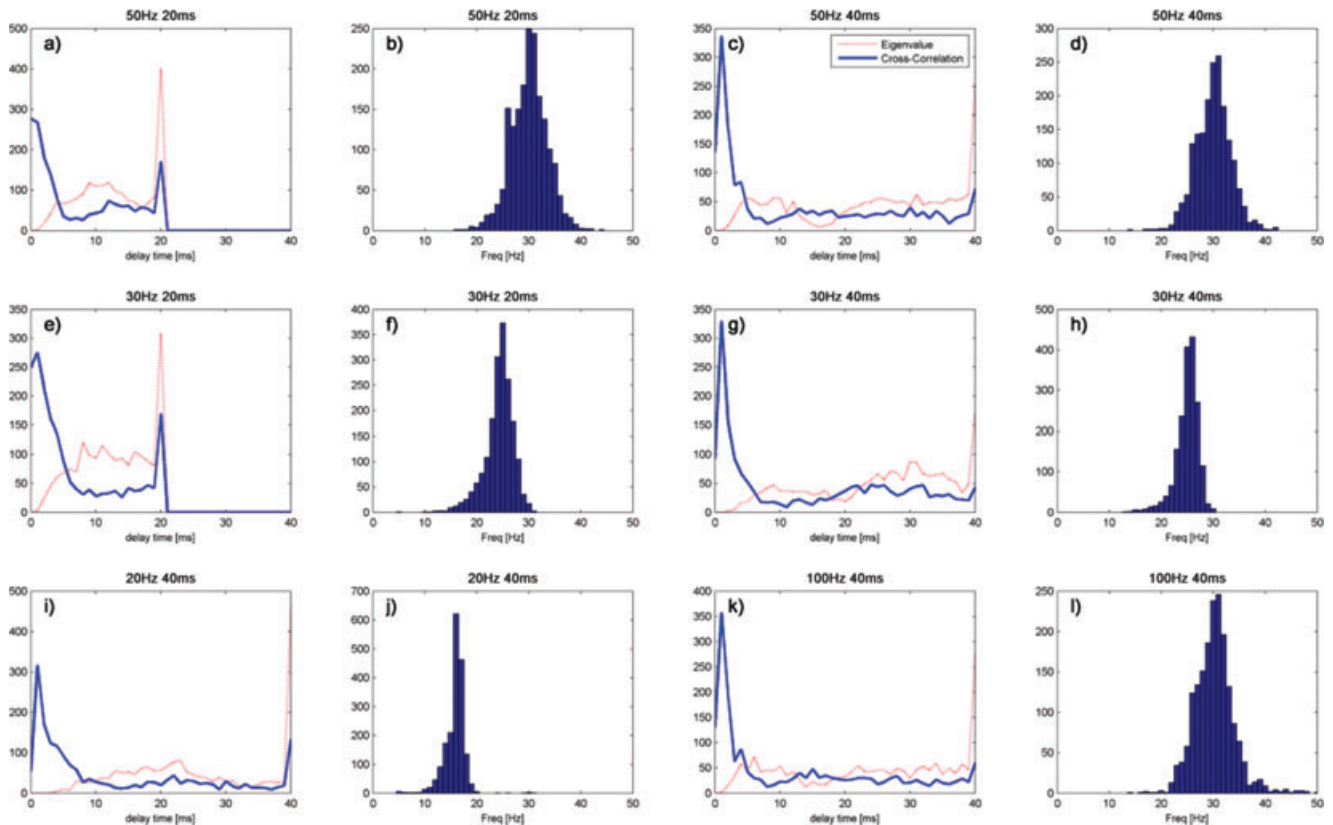

Figure 10 Distribution of delay times (first and third column) observed at the Valhall field for the EV (dashed) and XC method (solid) at the different parameters analysed. The *y*-axis for all plots shows the number or measurements within each bin. Note the large amount of very small XC delay times and maximum possible EV delay times for all parameters, representing null measurements. The peak at maximum XC delay times for $dt_{max} = 20$ ms indicates that this maximum delay is selected too short. Interestingly, there is a minimum in EV delay times at approximately 16 ms, which may indicate a cycle skipping effect for a signal with dominant frequency of 32 Hz. The histograms of dominant frequencies for each of the test (second and third column) show a peak at this frequency.
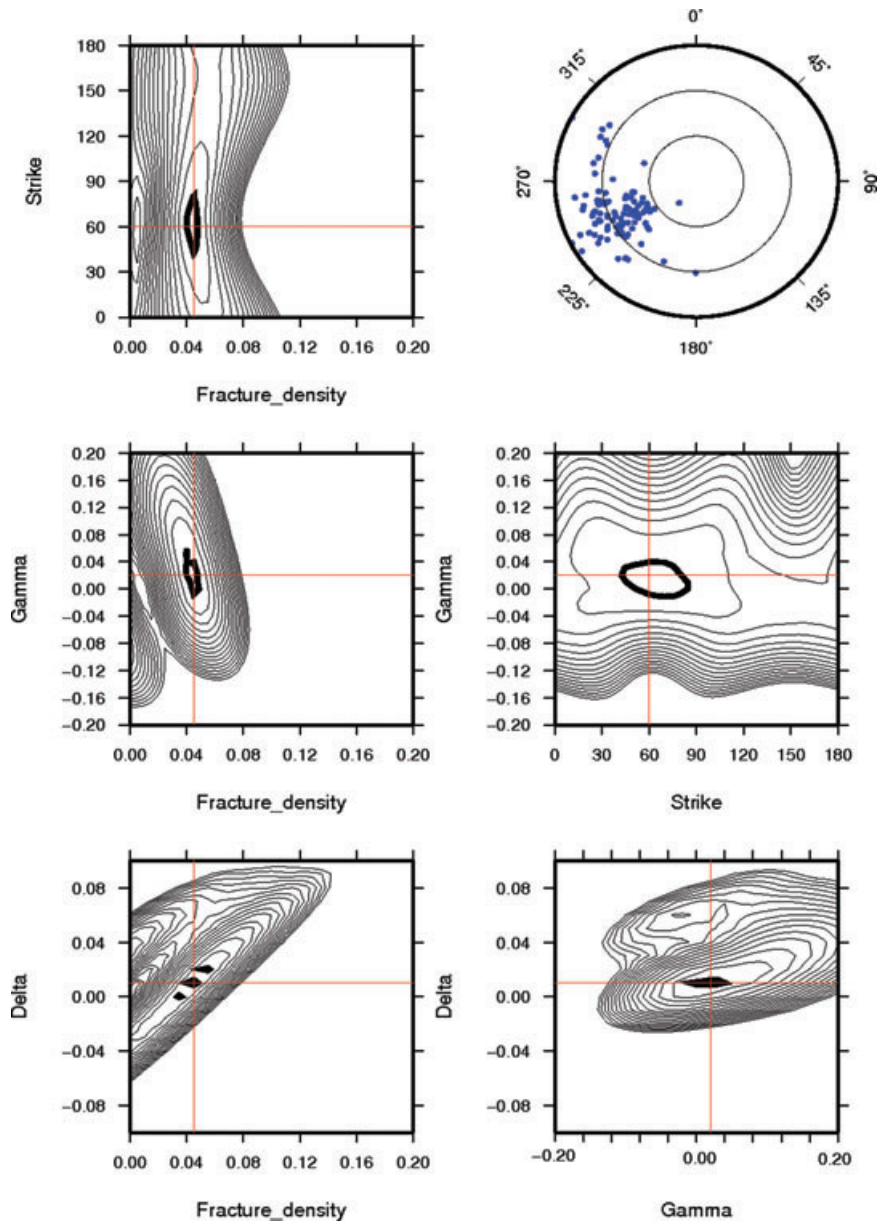
Figure 11 Inversion results for the Valhall North Sea oilfield in the same format as Fig. 9. This example shows the results for an upper filter frequency of 30 Hz, maximum delay time of 20 ms and a quality threshold of $\Gamma \geq 0.8$. See Fig. 9 for description and Table 2.

The splitting results are now inverted for VTI and HTI anisotropy. We use a quality threshold of $\Gamma = 0.80$ and the same additional error constraints as in the manual approach. The results are presented in Table 2 and replicate the results of the manual approach of Teanby *et al.* (2004b) for a filter of 30 Hz and restricting the maximum delay time to 20 ms. Figure 11 shows the error surface plots for that inversion. Note that the anisotropy parameters at Valhall show variation with frequency bands used. The fracture strike rotates

from N75°E at low frequencies to N170°E at broader bandwidths with fracture density, γ and δ slightly decreasing with increasing bandwidth. Exploring the details of that frequency dependence is beyond the scope of this paper.

SUMMARY

We have presented an automated method for shear-wave splitting analysis that provides an objective estimate of the

quality of the measurement. Based on characteristic differences between two splitting techniques the quality of a measurement can be determined robustly. As a result, good and null measurements can be easily distinguished. The best measurements are then used in an inversion routine to determine the anisotropy parameters of the rock mass. Here, we use this approach to infer dominant crack orientation and density as well as the strength of anisotropy caused by sedimentary fabrics.

This workflow may be extended in the future. Given a long enough recording period, the process may be applied to subsets of the data to analyse the temporal variation during observation/production. Furthermore, shear-wave splitting tomography will help isolating zones of anisotropy along the raypaths (e.g., Abt and Fisher 2008). However, this requires very good ray coverage, which is not yet available in most experiments. And finally, recent publications have demonstrated that frequency dependent shear-wave splitting may yield information about the actual fractures size and/or pore connectivity (e.g., Marson-Pidgeon and Savage 1997; Liu *et al.* 2006; Maultzsch *et al.* 2003; Brown and Gurevich 2004; Al-Anboori *et al.* 2005). The Chapman (2003) fracture model allows for pressure equalization from pore to crack to fracture scale, each of which should show different relaxation time scales and sensitivity to different frequencies of the wave and hence, a frequency dependent shear-wave splitting.

The automated shear-wave splitting technique presented in this paper enables processing of large data sets relatively cheaply. In production environments this automated processing may be used as a real-time monitoring tool. It may even be possible to apply this technique in real-time to laboratory and field shear experiments, to monitor fractures evolution ahead of rock failure.

ACKNOWLEDGEMENTS

REFERENCES

Abt D.L. and Fischer K.M. 2008. Resolving three-dimensional anisotropic structure with shear wave splitting tomography. *Geophysical Journal International* **173**, 859–886.

Al-Anboori A., Kendall J.M., Raymer D. and Jones R. 2005. Microseismic monitoring and spatial variations in anisotropy, an example from Oman. 67th EAGE meeting, Madrid, Spain, Expanded Abstracts.

Al-Harrasi O., Wuestefeld A. and Kendall J.M. 2009. Towards a fully automated shear-wave splitting analysis of microseismic data. 71st EAGE meeting, Amsterdam, the Netherlands, Expanded Abstracts.

Ando M., Ishikawa Y. and Wada H. 1980. S-wave anisotropy in the upper mantle under a volcanic area in Japan. *Nature* **286**, 43–46.

Backus G.E. 1962. Long-wave elastic anisotropy produced by horizontal layering. *Journal of Geophysical Research* **67**, 4427–4440.

Bokelmann G.H.R. and Baisch S. 1999. Nature of narrow-band signals at 2.083 Hz. *Bulletin of the Seismological Society of America* **89**, 156–164.

Brown L. and Gurevich B. 2004. Frequency-dependent seismic anisotropy of porous rocks with penny-shaped cracks. *Exploration Geophysics* **35**, 111–115.

Butler K.E. and Russelly R.D. 2003. Cancellation of multiple harmonic noise series in geophysical records. *Geophysics* **68**, 1083–1090.

Chapman M. 2003. Frequency-dependent anisotropy due to meso-scale fractures in the presence of equant porosity. *Geophysical Prospecting* **51**, 369–379.

Chevrot S. 2000. Multichannel analysis of shear wave splitting. *Journal of Geophysical Research* **105**, 21579–21590.

Crampin S. 1984. Effective anisotropic elastic constants for wave propagation through cracked solids. *Geophysical Journal of the Royal Astronomical Society* **76**, 135–145.

Crampin S. and Peacock S. 2008. A review of the current understanding of seismic shear-wave splitting in the Earth's crust and common fallacies in interpretation. *Wave Motion* **45**, 675–722.

Dricker I., Vinnik L., Roecker S. and Makeyeva L. 1999. Upper mantle flow in eastern Europe. *Geophysical Research Letters* **26**, 1219–1222.

Dyer B.C., Jones R.H., Cowles J.F., Barkved O.I. and Folstad P.G. 1999. Microseismic survey of a North Sea reservoir. *World Oil* **220**, 74–79.

Eisner L., Duncan P.M., Heigl W.M. and Keller W.R. 2009. Uncertainties in passive seismic monitoring. *The Leading Edge* **28**, 648–655.

Elkibbi M. and Rial J.A. 2005. The Geysers geothermal field: Results from shear-wave splitting analysis in a fractured reservoir. *Geophysical Journal International* **162**, 1024–1035.

Evans M.S., Kendall J.-M. and Willemann R.J. 2006. Automated SKS splitting and upper-mantle anisotropy beneath Canadian seismic stations. *Geophysical Journal International* **165**, 931–942.

Fukao Y. 1984. Evidence from core-reflected shear waves for anisotropy in the Earth's mantle. *Nature* **309**, 695–698.

Galvin R.J. Gurevich B. and Sayers C.M. 2007. Fluid-dependent shear-wave splitting in a poroelastic medium with conjugate fracture sets. *Geophysical Prospecting* **55**, 333–343.

Gao Y., Hao P. and Crampin S. 2006. SWAS: A shear-wave analysis system for semi-automatic measurement of shear-wave splitting above small earthquakes. *Physics of the Earth and Planetary Interior* **159**, 71–89.

Gibowicz S.J. and Kijko A. 1994. *An Introduction to Mining Seismology*. Academic Press. ISBN 0122821203.

Guest S., Van Der Kolk C. and Potters H. 1998. The effect of fracture filling fluids on shear-wave propagation. 69th SEG meeting, New Orleans, Louisiana, USA, Expanded Abstracts, 948–951.

Hall S.A., Kendall J.-M., Maddock J. and Fisher Q. 2008. Crack density tensor inversion for analysis of changes in rock frame architecture. *Geophysical Journal International* **173**, 577–592.

Hess H.H. 1964. Seismic anisotropy of the uppermost mantle under oceans. *Nature* **203**, 629–631.

Holmes G.M., Crampin S. and Young R.P. 2000. Seismic anisotropy in granite at the Underground Research Laboratory, Manitoba. *Geophysical Prospecting* **48**, 415–435.

Hudson J.A. 1981. Wave speeds and attenuation of elastic waves in material containing cracks. *Geophysical Journal of the Royal Astronomical Society* **64**, 133–150.

Jones G.A., Raymer D., Chambers K. and Kendall J.M. 2010. Improved microseismic event location by inclusion of *a priori* dip particle motion: A case study from Ekofisk. *Geophysical Prospecting* (in press).

Jurkevics A. 1988. Polarization analysis of three-component array data. *Bulletin of the Seismological Society of America* **78**, 1725–1743.

Kaarsberg E.A. 1968. Elasticity studies of isotropic and anisotropic rock. *Transactions of the Society of Mining Engineering* **241**, 470–475.

Kendall J.M. 1994. Teleseismic arrivals at a mid-ocean ridge: Effect of mantle melt and anisotropy. *Geophysical Research Letters* **21**, 301–304.

Kendall J.-M., Fisher Q. J., Covey-Crump S., Maddock J., Carter A., Hall S.A., *et al.* 2007. Seismic anisotropy as an indicator of reservoir quality in siliciclastic rocks. In: *Structurally Complex Reservoirs* (eds S. Jolley, D. Barr, J. Walsh and R.J. Knipe), pp. 123–136. Geological Society, London.

Kendall J.-M., Pilidou S., Keir D., Bastow I.D., Stuart G.W. and Ayele A. 2006. The Afar volcanic province within the East African rift system. In: *Mantle Upwellings, Melt Migration and the Rifting of Africa: Insights from Seismic Anisotropy* (eds G. Yirgu, C.J. Ebinger and P.K.H. Maguire), pp. 55–72. Geological Society, London.

Liu E., Crampin S., Queen J. and Rizer W. 1993. Behaviour of shear waves in rocks with two sets of parallel cracks. *Geophysical Journal International* **113**, 509–517.

Liu E., Chapman M., Zhang Z. and Queen J.H. 2006. Frequency-dependent anisotropy: effects of multiple fracture sets on shear-wave polarisations. *Wave Motion* **44**, 44–57.

Long M.D. and Van Der Hilst R.D. 2005. Estimating shear-wave splitting parameters from broadband recordings in Japan: A comparison of three methods. *Bulletin of the Seismological Society of America* **95**, 1346–1358.

Mainprice D. and Silver P.G. 1993. Interpretation of SKS-waves using samples from the subcontinental lithosphere. *Physics of the Earth and Planetary Interiors* **78**, 257–280.

Marson-Pidgeon K. and Savage M. 1997. Frequency-dependent anisotropy in Wellington, New Zealand. *Geophysical Research Letters* **24**, 3297–3300.

Maultzsch S., Chapman M., Liu E. and Li X. 2003. Modelling frequency-dependent seismic anisotropy in fluid-saturated rock with aligned fractures: Implication of fracture size estimation from anisotropic measurements. *Geophysical Prospecting* **51**, 381–392.

Menke W. and Levin V. 2003. The cross-convolution method for interpreting SKS splitting observations, with application to one and two-layer anisotropic earth models. *Geophysical Journal International* **154**, 379–392.

Nicolas A. and Christensen N.I. 1987. Formation of anisotropy in upper mantle peridotites – A review. In: *Composition Structure and Dynamics of the Lithosphere Asthenosphere System* (eds K. Fuchs and C. Froideveaux), pp. 111–123. AGU.

O'Connell R.J. and Budiansky B. 1974. Seismic velocities in dry and saturated cracked solids. *Journal of Geophysical Research* **193**, 3339–3356.

Pointer T., Liu E. and Hudson J.A. 2000. Seismic wave propagation in cracked porous media. *Geophysical Journal International* **142**, 199–231.

Restivo A. and Helffrich G. 1999. Teleseismic shear wave splitting measurements in noisy environments. *Geophysical Journal International* **137**, 821–830.

Savage M.K. 1999. Seismic anisotropy and mantle deformation: What have we learned from shear wave splitting. *Reviews of Geophysics* **37**, 69–106.

Sileny J. and Plomerova J. 1996. Inversion of shear-wave splitting parameters to retrieve three-dimensional orientation of anisotropy in continental lithosphere. *Physics of the Earth and Planetary Interiors* **95**, 277–292.

Silver P.G. and Chan W.W. 1991. Shear wave splitting and subcontinental mantle deformation. *Journal of Geophysical Research* **96**, 16429–16454.

Teanby N.A., Kendall J.-M. and Van Der Baan M. 2004a. Automation of shear-wave splitting measurements using cluster analysis. *Bulletin of the Seismological Society of America* **94**, 453–463.

Teanby N.A., Kendall J.-M., Jones R.H. and Barkved O. 2004b. Stress-induced temporal variations in seismic anisotropy observed in microseismic data. *Geophysical Journal International* **156**, 459–466.

Thomsen L. 1986. Weak elastic anisotropy. *Geophysics* **10**, 1954–1966.

Thomsen L. 1995. Elastic anisotropy due to aligned cracks in porous rock. *Geophysical Prospecting* **43**, 805–829.

Valcke S.L.A., Casey M., Lloyd G.E., Kendall J.-M. and Fisher Q.J. 2006. Lattice preferred orientation and seismic anisotropy in sedimentary rocks. *Geophysical Journal International* **166**, 652–666.

Vecsey L., Plomerová J., Kozlovskaya E. and Babuska V. 2007. Shear wave splitting as a diagnostic of variable anisotropic structure of the upper mantle beneath central Fennoscandia. *Tectonophysics* **438**, 57–77.

Vega S., Mavko G., Prasad M. and Nur A. 2006. Detection of stress-induced velocity anisotropy in unconsolidated sands. *The Leading Edge* **25**, 252–256.

Verdon J.P., Angus D.A., Kendall J.M. and Hall S.A. 2008. The effect of microstructure and nonlinear stress on anisotropic seismic velocities. *Geophysics* **73**, D41–D51.

Verdon J., Kendall J.-M. and Wuestefeld A. 2009. Imaging fractures and sedimentary fabrics using shear wave splitting measurements

made on passive seismic data. *Geophysical Journal International* **179**, 1245–1254.

Vidale J.E. 1986. Complex polarisation of particle motion. *Bulletin of the Seismological Society of America* **71**, 1511–1530.

Vinnik L.P., Kind R., Makeyeva L.I. and Kosarev G.L. 1989. Azimuthal anisotropy in the lithosphere from observations of long-period S-waves. *Geophysical Journal International* **99**, 549–559.

Wolfe C.J. and Silver P.G. 1998. Seismic anisotropy of oceanic upper mantle: Shear wave splitting methodologies and observations. *Journal of Geophysical Research* **B1**, 749–771.

Wuestefeld A. 2007. *Methods and applications of shear-wave-splitting: The East European craton*. PhD thesis, University Montpellier II, France.

Wuestefeld A. and Bokelmann G. 2007. Null detection in shear-wave splitting measurements. *Bulletin of the Seismological Society of America* **97**, 1204–1211.

Wuestefeld A., Bokelmann G., Zaroli C. and Barruol G. 2008. SplitLab: A shear-wave splitting environment in Matlab. *Computers and Geosciences* **34**, 515–528.

Zatsepin S.V. and Crampin S. 1997. Modelling of the compliance of crustal rock: I – Response of shear-wave splitting to differential stress. *Geophysical Journal International* **129**, 477–494.

APPENDIX: ADAPTIVE FILTERING OF PERIODIC NOISE

Periodic noise is a common problem in seismic records. 50 Hz is most common as it represents the transmission grid frequency. Some trains (also in mines) work on 16.7 Hz or 25 Hz. Higher frequencies can be introduced by overtones. Finally, some tool used in production or by nearby industries can cause a characteristic periodic noise (Bokelmann and Baisch 1999).

Butler and Russelly (2003) described a method to filter out multi-frequency stationary noise, aimed to cancel multiple harmonics of a dominant noise frequency. However, periodic noise frequencies may not be consistent for every recording of each sensor, perhaps due to varying sources of noise and/or beating as an artefact of resampling the seismogram in the preprocessing. We propose an adaptive multi-notch filter based on the Fourier transform of the autocorrelation of a noise window. The noise window is chosen to be from the start of the seismogram to 50 samples before the P-pick. An autocorrelation of the window ensures that any dominant frequencies are amplified and thus better detected than pure white noise. The frequency spectrum S_{Noise} of the noise is normalized to
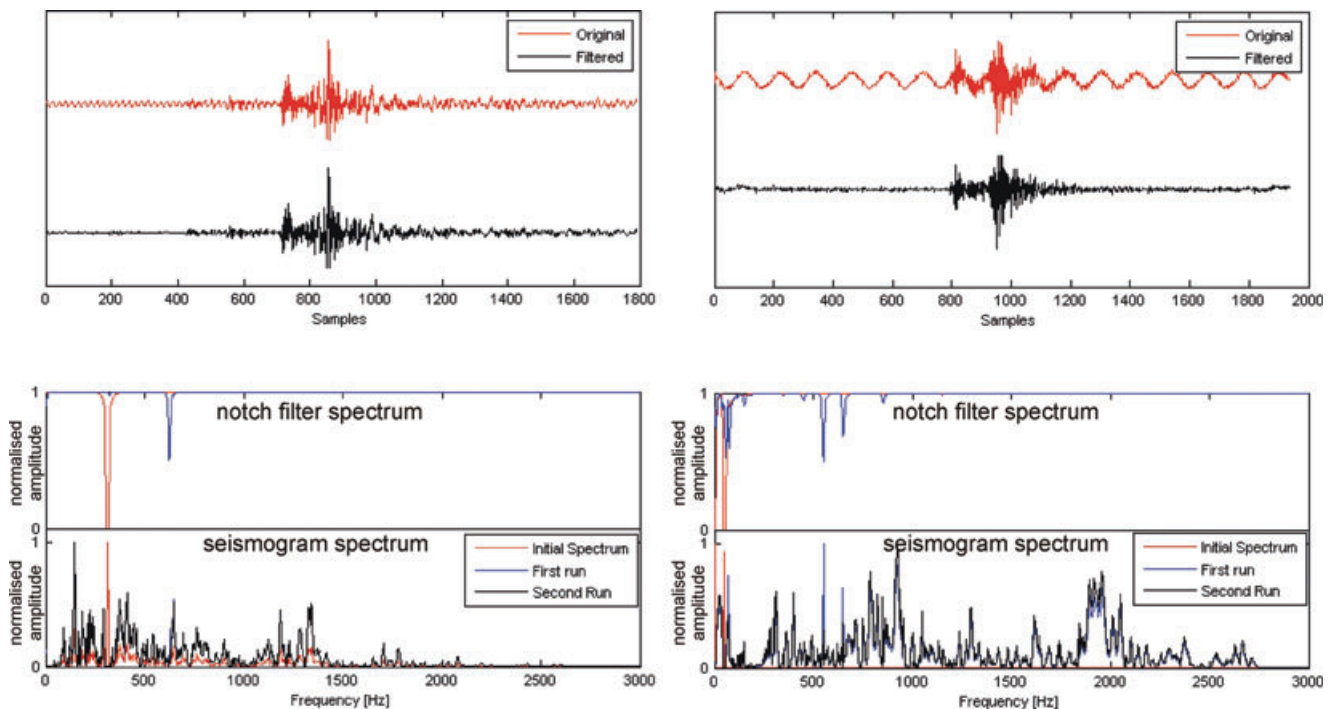

Figure A1 Examples of the self-adopting periodic frequency filter for two seismogram examples. Top panels show original (red) and filtered (black) seismograms. The lower panels show the normalized power spectrum for the different stages of filtering: initial (red), first run (blue) and final (black). The upper part of the panel represents the notch filter, a weighted filter factor *F* in frequency domain. Note that only spikes produced by periodic noise are filtered, whereas spikes in the signal part remain intact.

form a notch filter F

$$F = 1 - (S_{Noise} / \max(S_{Noise})). \qquad (6)$$

The filtered seismogram trace T is then the inverse Fourier transform of the product of the spectrum of the complete seismogram S_{Seis} multiplied by the filter F:

$$T = ifft(S_{Seis} \times F). \qquad (7)$$

Figure (A1) shows two examples of this filter. We found best results when applying this filter twice. More runs may be applicable in complex settings. Furthermore, different (decreasing) weighting factors ω for the filter can be applied in each step. This may ensure that the first dominant frequency is filtered out, whereas the remaining filters might detect signal-containing frequencies and thus must be damped less in order to maintain signal fidelity.